AIAA 80-1224R

Electromagnetic Propulsion: Drag and Erosion Modeling

Alfred C. Buckingham*
Lawrence Livermore National Laboratory, University of California, Livermore, Calif.

Railgun electromagnetic accelerators are being designed for hypervelocity projectile launch in equation-of-state impact experiments. Launcher development, with a goal of launching sabot-supported 1-*g* projectiles at speeds near 100 km/s, is proceeding in successive stages of increased acceleration and velocity. Some design problems include projectile aerodynamics during launch and free flight, plasma leakage past the projectile, stress deformation of rails and projectile, projectile and rail heating with attendant material erosion and drag, and the influence of these on launch ballistics. The influence of friction, drag and erosion on launch acceleration are emphasized in this paper. Included in the analysis is the measurement of sliding friction with concomitant projectile deformation. This is followed, where appropriate, with calculations of liquid-metal and multiphase (solid-particle and gas) erosive viscous-interface layer development with associated heat, mass, and momentum transport. Candidate dielectric projectile-materials, such as graphite and Teflon, as well as ablative sabot-coatings on steel projectiles are analyzed in the computational studies.

Nomenclature

A_s = projectile surface cross-sectional area
$a_{\mathcal{L}}$ = acceleration associated with Lorentz force
L_F = sliding coefficient of friction
C_P = specific heat at constant pressure
D_i^T = ith component thermal diffusion coefficient
$\mathfrak{D}_{ij}$ = species binary diffusion coefficient
H_T, h, h_i^0 = total, static, and ith species static datum enthalpy, respectively
j_i = ith species diffusion flux
K_i = ith component mass fraction
L, L^* = launch trajectory length, overall launcher length, respectively
m = mass of projectile
$\mathfrak{M}_i$ = ith species molecular weight
$\vec{N}_\perp$ = normal force, relative to projectile/rail interface
p = static pressure
$q, \dot{q}$ = thermal flux, combined thermal and mass transfer flux
r = radial coordinate relative to wall surface generation axis
R = gas constant
s = streamline coordinate tangent to wall surface
t = time
T = temperature
U, u = tangent streamline velocity component
v = normal to streamline velocity component
x_i = ith species mass concentration
y = normal to streamline velocity coordinate
Z_i, Z = ith component or mixture molecular compressibility, respectively
$\alpha_{k,i}$ = element and species proportionality fraction
Δ = incremental change
$\epsilon_D, \epsilon_M, \epsilon_H$ = turbulent eddy diffusion, viscosity, and thermal coefficients, respectively
ϕ_k = kth element production
ψ_i = ith species production
λ = molecular thermal conductivity
μ_i = $i = 1,2,3,4$ weighting coefficients for diffusive flux, Eq. (8)
τ_w = wall shear stress associated with a liquid/vapor viscous layer

Superscripts

$(\tilde{\ })$ = elemental average over associated species
$(\bar{\ })$ = mean average mixture quantity

Presented as Paper 80-1224 at the AIAA/SAE/ASME 16th Joint Propulsion Conference, Hartford, Conn., June 30-July 2, 1980; submitted Sept. 11, 1980; revision received April 20, 1981. This paper is declared a work of the U. S. Government and therefore is in the public domain.

*Physicist, Fluid Dynamics Continuum Mechanics Group, H-Division. Associate Fellow AIAA.

Introduction

THE long history of interest in magnetic propulsion was given additional impetus by the relatively recent successes of Rashleigh and Marshall,[1] Barber,[2] and Kolm.[3] Previous notions on the limitations of launch ballistics, erosion, and drag appear to have been overly pessimistic in light of the promising results of these investigators. In particular, the potential for achieving hypervelocity launch of very small projectiles has excited considerable interest at Lawrence Livermore National Laboratory (LLNL), Los Alamos National Laboratory (LANL), and other facilities, where high velocities are essential for material-impact shock-response studies of the dynamic physical properties of highly compressed matter. In the present work, we re-examine some of the previous assumptions, particularly those affecting laterally constrained launch ballistics, acceleration, and velocity limits.

The propulsion force in our launcher is applied to the base of the projectile (or its surrounding sabot) by a moving plasma layer that acts as a moving armature. The expanding current loop at the base of the projectile is completed, and the projectile is accelerated by the Lorentz force induced when the current and the magnetic field of the rail interact (Fig. 1). The design was described by Brittingham and Hawke.[4] Hawke and Scudder[5] evaluated material strength, plasma leakage, and initial estimates of erosion, drag, and ballistics problems of a laterally constrained magnetic launcher. Hawke[6] reported the initial designs associated with the initial phase of the collaborative LLNL/LANL test launches.

In this paper, we present the theoretical model developed for predicting drag, material erosion, and launch ballistics and their corresponding influence on selection of design materials and configurations. From our work, it appears that the primary reason for previous, somewhat pessimistic, estimates of excessive drag, frictional heating, and projectile failure was the lack of consideration about the mutual interaction between material- and fluid-dynamic responses

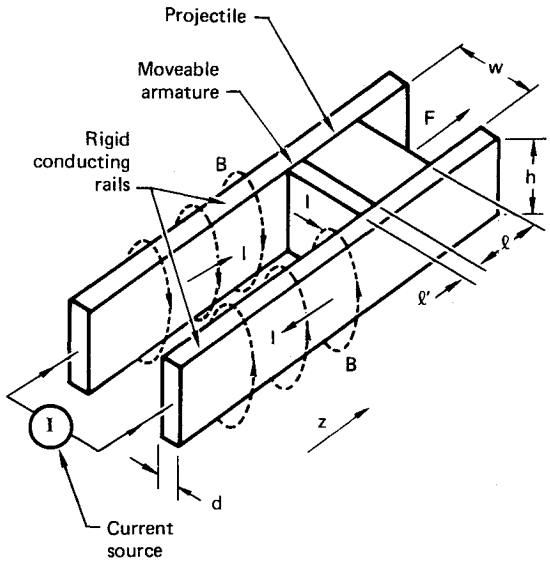

Fig. 1 Schematic of electromagnetic hypervelocity launcher illustrating conducting rails, rail field, and interaction with expanding current loop.

during the constrained launch phase. From our results, we predict an initial massive projectile rail loading due to plastic deformation of the sabot accelerated at an essentially constant, very high, level (up to 10^7 times the gravitational force) instead of simple contact friction. Here, we analyze the resulting deterioration of the metal-to-metal contact surface or, more realistically, the deterioration of the metal-to-nonmetal (dielectric) contact surface between the rail and projectile. The analysis includes the development and growth of a liquid metal, or erosion product, Couette-like viscous film layer (vapor to solid) intervening between rail and projectile surface. The viscous layer region is modeled as an unsteadily growing layer that entrains and expels erosion products, which develop at the projectile-to-rail surface during acceleration. The model necessarily includes the effects of multicomponent chemistry, particulates, multiphase transport, and turbulence.

In the analysis, the viscous flow and heating losses associated with a liquid metal (melting interface) and interface recession are first outlined and described. This phase follows contact heating to the melting threshold of the metal-to-metal (or metal-to-nonmetal) interface by high-speed frictional shear heating. In addition, we calculate the history of the ballistic launch cycle subject to these energy-loss and mass-removal considerations.

The total energy expended in accelerating a $1\times1\times0.5$-cm rectangular parallelepiped-shaped projectile (Fig. 2) is represented by the summation of frictional drag, heat, and mass transfer between projectile and rails plus the energy dissipated in melting or ablation of the guidance rails or projectile. In some of our studies, the projectile is considered completely enveloped by homogeneous sabot material.

For metal (steel) projectile-sabot material estimates, the thermodynamic, transport, and material properties of 4340 steel are used. The initial steel projectile-sabot mass is 3.75×10^{-3} kg. For carbon (graphite) and Teflon† ablative dielectric sabots, the appropriate (graphite or Teflon) properties are used. However, the accelerated initial mass for either material is somewhat less than the steel projectiles, about 1.2×10^{-3} kg. From the current source and plasma

†Reference to a company or product name does not imply approval or recommendation of the product by the University of California or the U. S. Department of Energy to the exclusion of others that may be suitable.

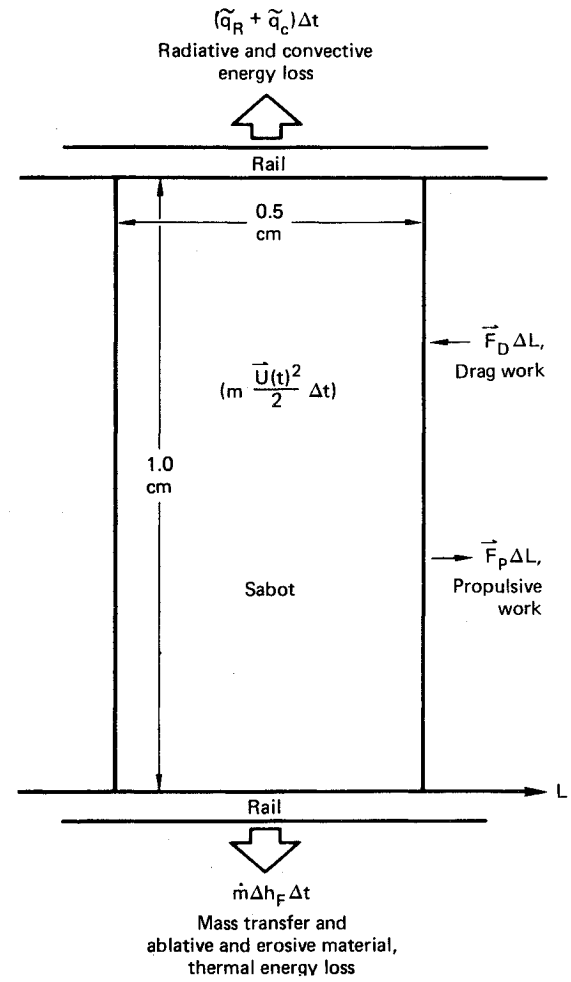

Fig. 2 Energy balance of the rail-constrained hypervelocity projectile.

estimates given in Hawke and Scudder,[5] we can compute the acceleration for the metallic sabot as:

$$a_{\mathfrak{L}} = 3.149\times10^7 \text{ m/s}^2$$

That for the graphite or Teflon sabot is

$$a_{\mathfrak{L}} = 9.842\times10^7 \text{ m/s}^2$$

Contributions to the energy balance include 1) propulsive energy accumulated from initiation of motion ($t=0$) until some time t' and accelerating the projectile to a velocity $U(t)$, with propulsive force, $F_p = m(t)a$; 2) the loss of mass of the projectile $m(t)$ continually reduced by erosive material loss due to friction and heating; 3) the kinetic energy of the projectile; 4) energy invested in the rate-of-change of the radiative, q_R, and convective, q_c, heating; 5) melting and vaporization energy Δh_f associated with the effected mass change m_F; and 6) shear-frictional loss computed as the product of the various components of wall friction force: Σ_w from liquid, solid, vapor boundary layer, and sliding friction.

Formulation

Viscous, Erosive, and Corrosive Contact Wall Layer

The contact friction of the metal-to-metal rail sabot was computed from an upper limit of the estimated normal force $\vec{F}_\perp$ and variable coefficient of sliding friction C_F. This coefficient is usually obtained from published low-speed sliding data and does not apply at high speed, because material degeneration (solid surface erosion and corrosion, melt, and thermal ablation) are present. In our model, we

treat the friction in sequential phases. The initial sliding-phase calculation is followed by calculations including liquid metal film layer or ablation and erosion (two phase) film layer, where appropriate. In the launch calculations, the normal force on the projectile is assigned a maximum value that corresponds to a strengthless material stressed beyond its yield limit. This value is that given by the projectile applying a force to the launcher rails equivalent to the plasma-acceleration force acting on its base.[5]

Calculations of the supplemental film layer or the liquid melt film layer are modeled with viscous-layer approximations applied to the Couette flow in the contact region. The melt layer is assumed to be removed as fast as it forms by entrainment of the liquid and its advection through the viscous boundary layer. Because a gap develops between eroding projectile and rails during launch, some configurations, particularly the metallic sabot, may fail well before they are completely consumed by erosive friction and heating. In our model, we assume this failure occurs when the gap reaches a size large enough to permit excessive plasma leakage past the projectile, reducing the thrust and destructively heating the rail-projectile surface interface.

The solutions of the Couette-flow viscous layer are modeled using the Bartlett-Kendall integral matrix code. This code solves the steady-state compressible boundary-layer equations for turbulent flow.[7,8] It includes nonequilibrium gas phase and gas-to-surface reaction kinetics as well as multispecies-component property models.[9-12]

The governing equations follow. The first description is that of the original Bartlett-Kendall formulation.[7] Following this, there is a discussion of some approximations made to account for the accelerating motion of projectile, plasma, and gas. Omitting radiation transport, the global-mass conservation, momentum, energy, and species conservation are, respectively,

$$\frac{\partial \rho u r^{\kappa}}{\partial s} + \frac{\partial \rho v r^{\kappa}}{\partial y} = 0 \tag{1}$$

$$\rho u \frac{\partial u}{\partial s} + \rho v \frac{\partial u}{\partial y} = \frac{1}{r^{\kappa}} \frac{\partial}{\partial y}\left[\rho r^{\kappa}(\nu + \epsilon_M)\frac{\partial u}{\partial y}\right] - \frac{\partial P}{\partial s} \tag{2}$$

$$\rho u \frac{\partial H_T}{\partial s} + \rho v \frac{\partial H_T}{\partial y} = \frac{1}{r^{\kappa}} \frac{\partial}{\partial y}\left[\rho r^{\kappa}(\epsilon_M + \nu)\frac{\partial u^2/2}{\partial y} + r^{\kappa}(\lambda + \rho \epsilon_H \tilde{C}_P)\frac{\partial T}{\partial y} + r^{\kappa}\sum_i \left(\rho \epsilon_D \frac{\partial K_i}{\partial y} - j_i\right) h_i - \frac{r^{\kappa} RT}{p} \sum_i \sum_j \frac{x_j D_i^T}{\mathfrak{M}_i \mathfrak{D}_{ij}}\left(\frac{j_i}{K_i} - \frac{j_j}{K_j}\right) + r^{\kappa} q_r\right] \tag{3}$$

$$\rho u \frac{\partial K_i}{\partial s} + \rho v \frac{\partial K_i}{\partial y} = \frac{1}{r^{\kappa}} \frac{\partial}{\partial y}\left[r^{\kappa}\left(\rho \epsilon_{D_i} \frac{\partial K_i}{\partial y} - j_i\right)\right] + \psi_i \tag{4}$$

$$H_T = h + \frac{u^2}{2} \qquad h = \sum_i K_i h_i \qquad h_i = \int_{T^0}^{T} C_{P_i} dT + h_i^0 \tag{5}$$

and $\kappa = 0,1$ for plane or axially symmetric flow, respectively.

The flux j_i for multicomponent diffusion is obtained from the Stefan-Maxwell relation,

$$\frac{\partial x_i}{\partial y} = \sum_j \frac{x_i x_j}{\rho \mathfrak{D}_{ij}}\left[\frac{j_j + D_j^T \frac{\partial InT}{\partial y}}{K_j} - \frac{j_i + D_i^T \frac{\partial InT}{\partial y}}{K_j}\right] \tag{6}$$

using the bifurcation approximation of Bird[11] and Bartlett et al.[12] In this procedure, the binary diffusion coefficient $\mathfrak{D}_{ij}$ is approximated by the function

$$\mathfrak{D}_{ij} \approx \frac{\bar{D}(T,P)}{F_i F_j} \tag{7}$$

where $\bar{D}$ is a reference diffusion coefficient and F_i a diffusion factor for species i. Then with a few of the following definitions,

$$Z_i \equiv \mathfrak{M}_i x_i / F_i \mu_2, \qquad \mu_i \equiv \sum_j x_j F_j, \qquad \mu_2 \equiv \sum_j \frac{\mathfrak{M}_j x_j}{F_j}$$

$$\mu_3 \equiv \sum_i \frac{Z_i}{i}, \qquad \mu_4 \equiv \ell n(\mu_2 T^{c_t}), \qquad c_t \approx -0.5$$

$$\tilde{C}_P \equiv \sum_i Z_i C_{P_i}, \qquad \tilde{h} \equiv \sum_i Z_i h_i \tag{8}$$

the Stefan-Maxwell equations can be solved explicitly for the diffusive flux; i.e.,

$$j_i = -\frac{\rho \bar{D} \mu_2}{\mu_1 \mathfrak{M}}\left[\frac{\partial Z_i}{\partial y} + (Z_i - K_i)\frac{\partial \mu_4}{\partial y}\right] \tag{9}$$

In addition, the diffusive energy flux can be expressed as

$$q_a = -\left\{\rho(\epsilon_M + \nu)\frac{\partial\left(\frac{u^2}{2}\right)}{\partial y} + (\lambda + \rho \epsilon_H \tilde{C}_P)\frac{\partial T}{\partial y} + \rho \epsilon_D\left(\frac{\partial h}{\partial y} - \tilde{C}_P \frac{\partial T}{\partial y}\right) + \frac{\rho \bar{D} \mu_2}{\mu_1 \mathfrak{M}} - \left[\frac{\partial \tilde{h}}{\partial y} - \left(\tilde{C}_p + \frac{c_t^2 R}{\mu_1 \mu_2}\right) \times \frac{\partial T}{\partial y} + c_t RT \frac{\partial \mu_3}{\partial y} + (\tilde{h} - h + c_t RT \mu_3)\frac{\partial \mu_4}{\partial y}\right]\right\} \tag{10}$$

For some problems (e.g., equilibrium chemistry) the number of differential equations to be solved can be reduced substantially if conservation of elements rather than conservation of species is used. Thus, if the elemental mass fraction is defined by

$$\tilde{K}_k = \sum \alpha_{ki} K_i \tag{11}$$

and

$$\tilde{Z}_k \equiv \sum_i \alpha_{ki} Z_i \qquad \phi_k \equiv \sum_i \alpha_{ki} \psi_i \tag{12}$$

the diffusive flux will be represented by

$$j_k = -\frac{\rho \bar{D} \mu_2}{\mu_1 \mathfrak{M}}\left[\frac{\partial \tilde{Z}_k}{\partial y} + (\tilde{Z}_k - \tilde{K}_k)\frac{\partial \mu_4}{\partial y}\right] \tag{13}$$

and the elemental species conservation equation becomes

$$\rho u \frac{\partial \tilde{K}_k}{\partial s} + \rho v \frac{\partial \tilde{K}_k}{\partial y} = \frac{1}{r^{\kappa}} \frac{\partial}{\partial y}\left[r^{\kappa}\left(\rho \epsilon_D \frac{\partial \tilde{K}_k}{\partial y} - j_k\right)\right] \tag{14}$$

Because elements are conserved,

$$\sum_j \alpha_{ij} \psi_j = 0$$

and would not be appropriate for nonequilibrium chemistry, since the production terms vanish. However, by reintroducing the production terms in this conservation equation, the same formulation can be used for equilibrium or nonequilibrium chemistry by simply setting the production terms to zero for equilibrium conditions.

The turbulence-model closure is by a simple algebraic eddy-viscosity representation. This reduces the solution procedure complexity as much as possible, while the variety of other complications, such as multicomponent and multiphase effects, are treated in detail. Additional turbulent code-model refinements were developed and applied in special formulations of the Bartlett-Kendall code in erosive flow studies. The refinements included the effects of exterior (core flow) generated turbulence, intermittency, and large scale unsteady turbulence structures. Discussion of these features and their mathematical development appeared in previous publications; see, for example, Buckingham.[13]

The set of boundary conditions for the viscous melt-layer or gaseous boundary-layer consists of the specification of initial profiles for the dependent variables, i.e., velocity, enthalpy, and, if applicable, species composition and concentrations. In addition, the set contains specifications of these quantities along the wall and at the edge of the viscous layer. To these we add specifications for the eroding wall, including effects of wall melting, vaporization, and advection and transport of eroded surface material.

We must also approximate the unsteady boundary conditions from the accelerating projectile and gas and then match them to the detailed boundary-layer solutions. Coarsely zoned unsteady solutions of the Navier-Stokes equations are first obtained for the entire region of viscous and inviscid flow between projectile and rails. The solutions are used to establish the relative growth of the viscous boundary-layer region at various times and stream-related positions. The detailed Bartlett-Kendall code is subsequently applied, with a point-to-point stream-related patch, to the Navier-Stokes results.[12] This patching procedure impresses values of the acceleration $\partial \vec{U}_e/\mathrm{d}x$ at a succession of stream-related stations. The unsteady Navier-Stokes results supply information on the relative variation in viscous layer thickness in both space and time and the corresponding histories of stream-related mass entrainment. This quasitransient patch approximation is based on applying the linear Euler approximation for uniformly accelerating flow,

$$\frac{\partial \vec{U}_e}{\partial t} \simeq \vec{U}_e \frac{\partial U_e}{\partial x} \tag{15}$$

The viscous-layer rate of growth and its influence on the viscous profiles, heat and mass transfer, and surface erosion is approximated by scaling the normal to the surface spatial coordinate (y) in the boundary-layer solutions by

$$\eta = \int_0^{y^*} \frac{\rho(y)}{\rho_e} \frac{\mathrm{d}y}{2\sqrt{\nu t}} \tag{16}$$

In Eq. (15) $\vec{U}_e$ is the mean velocity. This velocity represents, in our Couette analogy, the instantaneous projectile speed. Physical time is represented by t, $\rho(y)$ is the density profile computed in the boundary-layer solutions, and ρ_e is the edge density. The physical coordinate (y) is taken to be zero at the stationary rail and is $y_e = \delta$, the gap thickness, at the moving projectile. The kinematic viscosity ν is the ratio of the local viscosity coefficient to the mass density. This patch procedure currently is being replaced by development of a fully time-dependent code for modeling the accelerating projectile erosion. Although solutions for nonreactive single-phase turbulent flow have been obtained using the new code, the multicomponent and multiphase influences will require additional time to implement. For this reason, we apply the foregoing quasitransient approximations throughout this early phase of the rail launcher design.

Here, we introduce considerations about laminar vs turbulent flow before discussing current results. Although our calculations are made primarily for fully-developed turbulent flow, a few results (i.e., much less erosion, drag, and heating) for laminar flow are shown for comparison, because we believe the estimates for turbulent flow may be conservative. Under accelerations, such as encountered in railgun launch, the turbulence is not expected to fully develop in the boundary layer. There is evidence that even fully-developed turbulent boundary layers will regress to the laminar state when the acceleration exceeds a critical value, which is surpassed in the unsteady history of a railgun launch.[14-16] The railgun launcher experiments appear as an ideal framework for conducting detailed examination of this possibly significant decrease in erosive drag effects under conditions of hypervelocity acceleration.

The results of our sequence of boundary-layer Couette-flow model calculations (more than 30) are summarized as correlations. These are given as simple polynomials or in exponential regression form based on the numerical simulation data. The correlation functions were then programmed into the trajectory calculations, which are numerical integrations of the energy balance represented in Fig. 2. The launch-phase projectile motions are discussed in the next section.

Equations of Rail Constrained Motion

For the energy balance (Fig. 2) and its influence on the launch drag and ballistics, we consider contributions from the frictional drag, projectile and rail heat transfer, mass transfer, phase change, and ablation and erosion as the total drag debt paid by the available propulsion energy. The resulting energy-balance equation is expressed in the following (integral work) form for programming:

$$U_p(t+\Delta t) - U_p(t) = a_{\mathfrak{L}} \Delta t - C_F \int_t^{t+\Delta t} \frac{\vec{N}_\perp(t)}{m(t)} \mathrm{d}t$$

$$- A_s \left\{ \int_t^{t+\Delta t} \frac{\tau_w(t)}{m(t)} \mathrm{d}t + \int_t^{t+\Delta t} \frac{\dot{q}(t)}{m(t)\, U_p(t)} \mathrm{d}t \right\}$$

$$- \int_{m(t)}^{m(t+\Delta t)} U_p[m(t)]\, \mathrm{d}m \tag{17}$$

subject to the conditions $a_{\mathfrak{L}}$, C_F, $A_s \simeq$ const, $U_p(L=0, t=0)=0$, $m(L=0, t=0)=m_0$. The calculations terminate at $t=t_F$ where the launcher length L^*, specified as a design parameter, is equivalent to the distance traversed by the projectile,

$$L^* = \int_{t=0}^{t=t_F} U_p(t)\, \mathrm{d}t \tag{18}$$

Equation (17) is programmed to integrate over selected time increments (δt) at automatically controlled intervals. The nonlinear contributions of velocity change, mass change, and effects on heat, mass, momentum, and thermochemical state changes are combined with an implicit (iterative) algorithm applied at each time step. Time step control is imposed using a periodic Jacobian evaluation for derivative magnitudes. This is necessary because of the inherent stiffness of Eq. (17), which occasionally develops from the imbalance in relaxation times between accelerations, $\mathrm{d}U_p/\mathrm{d}t$, and mass changes, $\mathrm{d}m/\mathrm{d}t$.

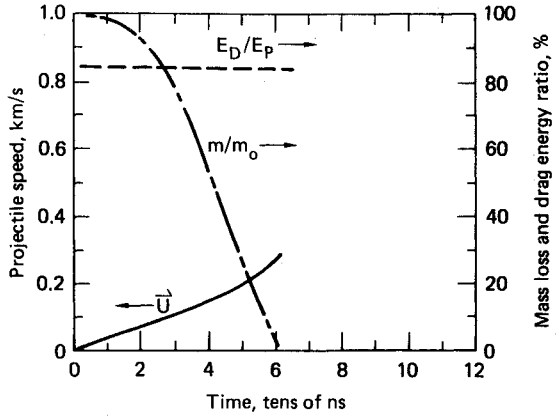

Fig. 3 Projectile launch history considering continuous sliding contact, metal-to-metal friction, and melt, exclusively.

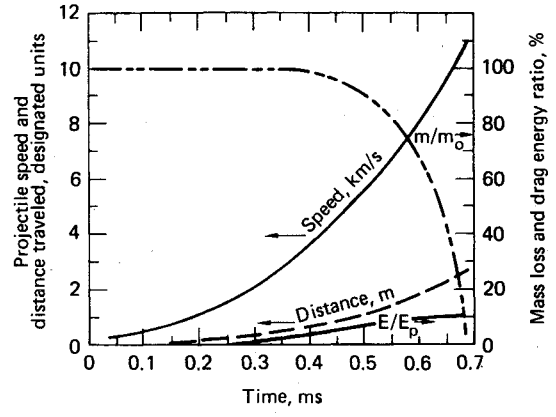

Fig. 4 Projectile launch history of initial sliding contact period followed by surface melt with viscous drag and heating loss.

Results and Analysis

The most pessimistic estimate of electromagnetic railgun launch is obtained by assuming projectile surface-to-rail contact is maintained throughout the launch cycle. Moreover, the normal contact force is assumed to be the maximum mean-pressure exerted by the driving field arising from the plasma armature-sheath at the projectile base. The projectile is strengthless in this limiting assumption and, so, delivers an isotropic mean stress to the rails. The resulting drag and heating losses are the maxima for the acceleration prescribed (illustrated in Fig. 3), and only a short distance is traveled by the projectile before the mass is exhausted (consumed) by erosive heating and transport.

Significantly better performance is obtained by a more reasonable model, in which the slide and melt and vaporization phase is followed by Couette and boundary-layer friction and heating phases during the remainder of the launch period (Fig. 4). In this case, the gap conceptually grows sufficiently, so that the sum of the normal momentum, due to mass transfer from the melting surface, and the momentum integral, taken over the boundary-layer gap, balance and equilibrate the normal force $F_\perp$. At this time, and later in the particular launch event, the results of drag, heat transfer, and erosion are computed using the Couette-flow boundary-layer model for liquid metal (steel). The results (Fig. 4) are still not favorable for steel sabots. However, the use of other high-temperature materials (particularly, ceramic dielectrics), perhaps in combination with sacrificial ablative bands surrounding them, remains promising.

After film layer formation, Couette-flow calculations are used to model the erosive heat transfer and drag, either for the final liquid-metal layer predictions (Fig. 4) or for the erosive graphite and Teflon calculations, discussed later. The

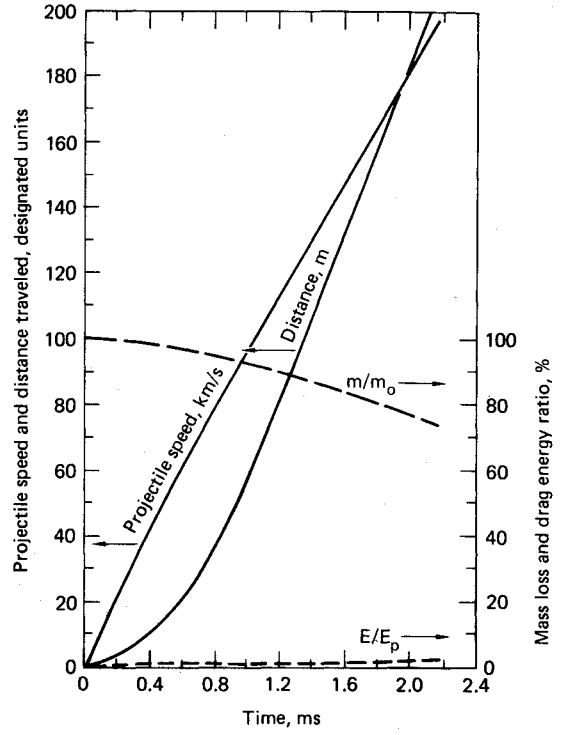

Fig. 5 Projectile launch history of ablative graphite-sabot sliding contact followed by two-phase erosive viscous-drag and heating loss.

boundary-layer and Couette-flow model includes variable mass density, state, equilibrium and chemically frozen transport properties, molecular erosive components, and solid phase (carbon) constituents of the eroding surfaces with modeled turbulent shear and mixing, where appropriate.

The results of the Couette-flow calculations indicate some improvement in performance using either graphite or plastic sabots instead of pure metal projectile-to-rail contact. However in either case (sabot or pure metal), failure of the concept may be realized from excessive leakage of the plasma (too large a gap), as opposed to the relatively minor mass loss. Certainly for the launcher experiments, even without an initial clearance (gap), the graphite or Teflon sabots are much more promising than the pure metal (steel) for reducing drag and material erosion.

The results for assumed turbulent boundary-layer (conservative) estimates are summarized for the graphite projectile (Fig. 5) and for the Teflon projectile initially confined (no gap) by the normal force equivalent to the acceleration force (Fig. 6). Ratios of mass (m/m_0) and energy (E/E_p), or drag work, for either Teflon or graphite are much more favorable than the pure steel sabot results, previously presented. Also, the launch trajectory parameters, distance vs time and velocity vs time, are depicted for the two projectile materials.

In addition, we investigated the influence of a modest amount of initial gap provided between the sabot and the rails. Conceptually, no sliding friction is developed; hence, only erosive boundary-layer drag, heat transfer, and mass transfer are associated with the drag energy expenditure during launch. We assume (conservatively) the initial sabot-to-rail clearance is occupied with 1 atm of ablation products. We then calculate, from this initial state, both the increased rate of mass loss of sabot erosion-products and the variable drag itself.

In Figs. 7 and 8 are plots of the laminar and turbulent total drag-energy in proportion to the propulsive energy for graphite and Teflon sabots at 100- and 200-m launch positions, respectively. The abscissa in each figure reflects the initial gap clearance assumed in the calculations. These results are the most promising of all. Even a modest (1-mil, 2.54×10^{-5}-m) initial clearance should be adequate to prevent

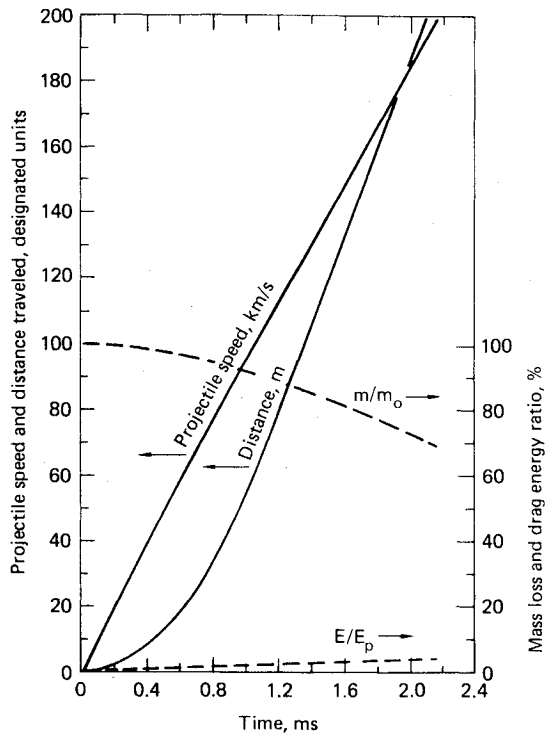

Fig. 6 Projectile launch history of ablative Teflon-sabot sliding contact followed by vapor-phase erosive viscous-drag and heating loss.

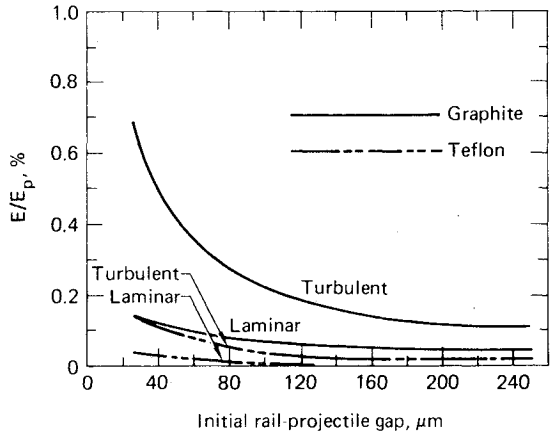

Fig. 7 Drag and heating-energy loss as a percentage of propulsive energy for a 100-m rail launch-position, with specified initial projectile-to-rail clearance gap.

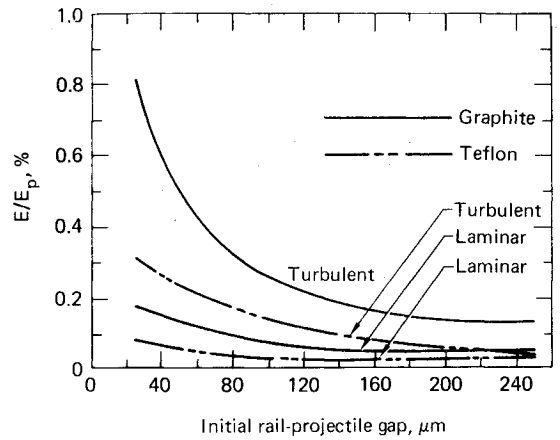

Fig. 8 Drag and heating-energy loss as a percentage of propulsive energy for a 200-m rail launch-position, with specified initial projectile-to-rail clearance gap.

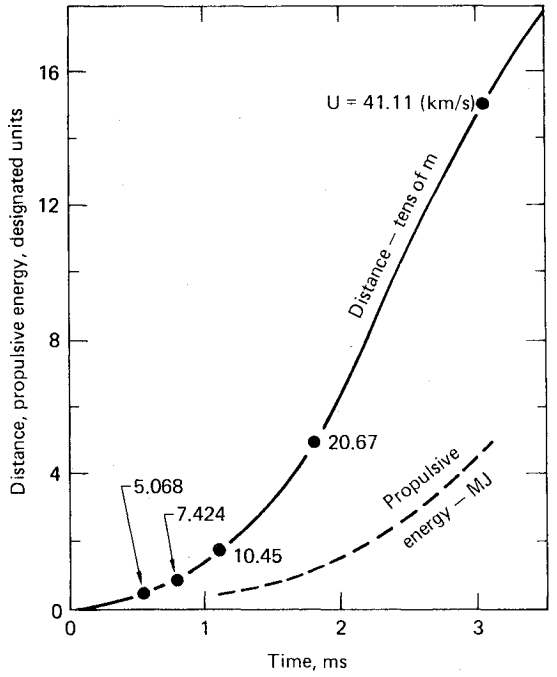

Fig. 9 Reference launch-time history, drag-free 3.75×10^{-3}-kg projectile distance, speed, and expended propulsive energy.

excessive drag. An additional problem develops, however, when a clearance gap is used; this is the possibility that oscillation and impacts will occur between sabot and rails during launch. A design answer may be to use ablative bands. These bands can act to effectively seal the gap, while they provide a high-pressure cushion between rails and projectile by permitting development of an ablative-product layer in the space between successive bands.

The base-state situation, drag-free launch (Fig. 9), is used to compare and analyze energy expenditure and trajectory variations using realistic drag and energy loss contributions.

Summary and Conclusions

We estimated possible hypervelocity launch in excess of 100 km/s for small projectiles ($\simeq 1$ *g*, encased in a disposable dielectric sabot). The projectiles can be accelerated by an electromagnetic force. The force develops by applying a constant current source driving a growing current loop closed at the accelerating projectile base by a thin plasma sheath. Previous estimates of drag, heating, material erosion, and sabot deterioration may have been excessively conservative, based on the implications drawn from our model calculations. However, experimental data must be obtained from a systematic study of repeated test launches. To help confirm these implications, the test launches must be instrumented for detecting, at least, material stress and strain, surface recession, and heat transfer rates. The essential difference between our results and previous estimates on the launch drag and erosion appears to be that we include in our calculations the effects of the eroding ablative and, in some cases, chemically-reactive rail-to-projectile film interface.

Provision of even a modest amount of initial gap between guidance rails and sabot is predicted to further insure the successful launch of ablation-layer coated (carbon-to-carbon and plastic) sabots. Recent experiments at somewhat lower (albeit hypervelocity) launch conditions ($\simeq 6$ km/s) verify that railgun launch of hypervelocity projectiles is possible and practical.

Additional experimental evidence of successful hypervelocity launches of projectiles in 1- and 2-m prototype railguns is also offered in support of our view of the potential

for this electromagnetic propulsion application. These first experiments were conducted at the LANL in November 1979 and February 1980 by a joint team of LANL and LLNL scientists. Although the railgun itself is undergoing material damage and metallurgical examination at the time of this writing, the evidence of successful launch of intact projectiles up to Mach 15 is considered a substantial support for continuing development of this launcher concept.

Acknowledgment

This work was performed under the auspices of the U. S. Department of Energy by Lawrence Livermore National Laboratory under Contract W-7405-Eng-48.

References

[1] Rashleigh, S. C. and Marshall, R. A., "Electromagnetic Acceleration of Macroparticles to High Velocities," *Journal of Applied Physics,* Vol. 49, April 1978, p. 2540.

[2] Barber, J. P., "The Acceleration of Macroparticles and a Hypervelocity Electromagnetic Accelerator," Ph.D. Thesis, Australian National University, Canberra, Australia, 1972.

[3] Kolm, H. H., "Basic Coaxial Mass Driver Reference Design," *Proceedings of the 3rd Princeton AIAA Conference on Space Manufacturing Facilities,* May 1977.

[4] Brittingham, J. N. and Hawke, R. S., "Magnetic Gradient Accelerators for Launching 0.1-g Payloads at Velocities Greater than 150 km/s," Lawrence Livermore National Laboratory, Livermore, Calif., UCRL-52778, May 1979.

[5] Hawke, R. S. and Scudder, J. K. "Magnetic Propulsion Railguns: Their Design and Capabilities," *Second International Conference on Megagauss Magnetic Field Generation and Related Topics,* Washington, D. C., May-June 1979.

[6] Hawke, R. S., "Railgun Accelerators for Launching 0.1 g Payloads at Velocities Greater than 150 km/s," *Proceedings of DOE Sponsored Impact Fusion Workshop,* Los Alamos National Laboratory, Los Alamos, New Mex., July 1979.

[7] Kendall, R. M. and Bartlett, E. P., "Nonsimilar Solution of the Multi-Component Laminar Boundary Layer by an Integral Matrix Method," *AIAA Journal,* Vol. 6, June 1968, pp. 1089-1097.

[8] Anderson, L. W. and Kendall, R. M., "A Nonsimilar Solution for Multicomponent Reacting Laminar and Turbulent Boundary Layer Flows Including Transverse Curvature," AFWL TR-69-106, March 1970.

[9] Bartlett, E. P., Kendall, R. M., and Rindal, R. A., "Further Studies of the Coupled Chemically Reacting Boundary Layer and Charring Ablator, Part I, Summary Report," Aerotherm ACUREX Corp., Mountain View, Calif., Rept. 68-38, Oct. 1968.

[10] Kendall, R. M., "An Analysis of the Coupled Chemically Reacting Boundary Layer and Charring Ablator, Part V: A General Approach to the Thermochemical Solution of Mixed Equilibrium - Nonequilibrium, Homogeneous or Heterogeneous Systems," NASA CR-1064, 1968.

[11] Bird, R. B., "Diffusion in Multicomponent Gas Mixtures," 25th Anniversary Congress, Society of Chemical Engineers (Japan), Nov. 1961.

[12] Bartlett, E. P., Kendall, R. M., and Rindal, R. A., "A Unified Approximation for Mixture Transport Properties for Multicomponent Boundary Layer Applications," Aerotherm ACUREX Corp., Mountain View, Calif., Aerotherm Final Rept. 66-7, Part IV, March 1967.

[13] Buckingham, A. C., "Propellant Driven Turbulent Interior Ballistics and Wall Erosion," Lawrence Livermore National Laboratory, Livermore, Calif., UCRL-81289, Nov. 1978; also, AIAA Paper 79-0007, New Orleans, La., Jan. 1979.

[14] Launder, B. E., "Laminarization of the Turbulent Boundary Layer in Severe Acceleration," *Journal of Applied Mechanics,* Vol. 31, Dec. 1964, p. 707.

[15] Moretti, P. M. and Kays, W. M., "Heat Transfer through an Incompressible Turbulent Boundary Layer with Varying Free Stream Velocity and Varying Surface Temperature," Stanford University, Thermo-Sciences Div., Palo Alto, Calif., PG-1, 1965.

[16] Schraub, F. A. and Kline, S. J., "A Study of the Structure of the Turbulent Boundary Layer with and without Longitudinal Pressure Gradients," Stanford University, Thermo-Sciences Div., Palo Alto, Calif., MD-12, 1965.